Hyperpolarized Xe-129 3D-Single Breath Chemical Shift Imaging

---

A Thesis Presented to

the faculty of the School of Engineering and Applied Science

University of Virginia

In Partial Fulfillment

of the Requirements for the Degree

Master of Science in Biomedical Engineering

By

Steven Guan

November, 2015

Approval Sheet

The thesis is submitted in partial fulfillment of the requirements

for the degree of

Masters of Science

_____

Author

The thesis has been read and approved by the examining committee:

Jaime Mata, Ph.D.

Advisor

Craig Meyer, Ph.D.

Committee Chair

John P. Mugler III, Ph.D.

Accepted for the School of Engineering and Applied Science:

Craig H. Benson, Dean, School of Engineering and Applied Sciences

December, 2015

Acknowledgements

The work presented here was only possible with the guidance and support from my advisor, committee, friends, and family.

I would like to thank my advisor, Dr. Jaime Mata, who has given me a unique opportunity to challenge myself and grow in both intellect and character. His faith in my abilities and persistence in achieving excellence has played a pivotal role in the completion of this project.

I would also like to thank Dr. John P. Mugler III and Dr. Craig Meyer from my committee for their critique and keen insight, which have strengthened my research as a whole.

I am grateful for Dr. Kun Qing, and his willingness to teach me the basics of MRI and data processing. I would not have been able to accomplish as much as I have without his guidance.

Finally, I cannot thank my family and friends enough for their support and encouragement.

Table of Contents

Abstract

Magnetic resonance imaging (MRI) is in general, capable of providing an immense amount of structural and functional information. Proton MRI in the lungs is challenging due to the inherently low water density and short T_2* in lung tissues compared to other tissues in the human body. However, there has been progress in proton MRI of the lungs using ultra-short echo time sequences to overcome these challenges. An alternative to proton imaging is hyperpolarized (HP) gas imaging, which uses Xenon-129 (Xe-129) and Helium-3 (He-3) as inhaled gaseous contrasting agents, and has allowed for unique approaches in evaluating lung structure and function. In this work, we demonstrated the feasibility of 3D Single Breath Chemical Shift Imaging (3D-SBCSI) for assessing regional lung ventilation and gas uptake and exchange in 3D within a single breath hold (less than 10 seconds). Having this regional information of the lungs may allow for a better understanding of disease progression. Additionally, we present a post-processing software package termed “Tools for Automated Spectral Processing” (TASP) for the automated processing and quantification of 3D-SBCSI data.

In this study, a total of 17 subjects including: 6 healthy, 8 interstitial lung disease (ILD), and 3 lung cancer (LC) subjects underwent 3D-SBCSI. To visualize the regional exchange of Xe-129 from the alveoli into the tissue and red blood cell (RBC) compartments, ratio maps of Tissue/Gas and RBC/Gas were generated. Tissue/RBC maps were also generated to visualize the Xe-129 exchange between the tissue and RBC compartments. Healthy subjects showed a uniform distribution of gas signal intensities and Tissue/RBC ratios throughout the lungs, whereas ILD subjects showed a heterogeneous distribution. Moreover, ILD subjects had a significantly higher mean Tissue/RBC than healthy subjects. One of the advantages of 3D-SBCSI was that it acquired the whole spectrum for each voxel, which allowed for the identification of previously unknown MR spectral peaks. With this technique, a new peak was identified in a lung cancer subject. This new peak was found to be associated with the presence of a tumor.

List of Abbreviations

3D-SBCSI	3D Single Breath Chemical Shift Imaging
CT	Computed Tomography
CSI	Chemical Shift Imaging
D_LCO	Lung Diffusing Capacity for Carbon Monoxide
FEV1	Forced Expiratory Volume in 1 Second
FID	Free-Induction Decay Signal
FVC	Full Vital Capacity
He-3	Helium-3
HP	Hyperpolarized
HRCT	High Resolution Computed Tomography
ILD	Interstitial Lung Disease
IPF	Idiopathic Pulmonary Fibrosis
LC	Lung Cancer
MRI	Magnetic Resonance Imaging
PFTs	Pulmonary Function Tests
PPM	Parts per Million
RBCs	Red Blood Cells
RF	radio frequency
SNR	Signal to Noise Ratio
T2*	Transverse Relaxation Time including effects of field inhomogeneity
TASP	Tools for Automated Spectral Processing
TE	Echo Time
Xe-129	Xenon-129

List of Figures and Tables

Chapter 1: Hyperpolarized Xenon-129 and 3D-SBCSI

1.A. Introduction

Magnetic resonance imaging (MRI) is a non-invasive imaging modality that can provide an immense amount of structural and functional information of the body. Unlike X-ray and computed tomography (CT), MRI does not expose the patient to any harmful radiation and can be used safely in pediatric populations [1]. Nevertheless, MRI is not widely used in clinical lung imaging due to the difficulty in acquiring high quality diagnostic images [2]. The origin of this problem lies in the fact that the lung has an inherently low water density and short T_2^*, which results in images with a poor signal to noise ratio (SNR). Normally, longer MRI sequences with more averages can be used to overcome SNR challenges. However, this is not feasible in breath-hold lung MRI because patients cannot hold their breath longer than 20-30 seconds. Sequences longer than a breath hold require some form of respiratory gating to minimize motion artifacts [3]. Despite these challenges, there has been progress in obtaining high quality diagnostic images of the lungs with ultra-short echo time proton MRI sequences [4].

An attractive alternative to proton MRI for clinical lung imaging is hyperpolarized (HP) gas imaging with Helium-3 (He-3) or Xenon-129 (Xe-129) as inhaled gaseous contrasting agents. Laser-based polarization devices can increase the nuclear polarization of He-3 and Xe-129 by a factor of 10,000 relative to their polarization at thermal equilibrium in a typical clinical MR scanner. By having a large nuclear polarization, they can be easily detected with an MR scanner tuned to the appropriate resonant frequency [5]. Hyperpolarized gas imaging overcomes the SNR challenge faced in proton MRI and allows for the direct imaging of lung airspaces. In this work, we demonstrate the feasibility of 3D Single Breath Chemical Shift Imaging (3D-SBCSI) for assessing regional lung ventilation and gas uptake and exchange in 3D within a single breath hold (less than 10 seconds).

1.B. Hyperpolarized Gas Imaging with Xenon-129

HP gas imaging has enabled many unique approaches for evaluating lung structure and function with HP He-3 and Xe-129 as inhaled gaseous contrasting agents. While the applications of He-3 have been well demonstrated, it is not widely used due to its limited supply and rising price [6-10]. For these reasons, Xe-129 has become an attractive alternative with an effectively unlimited supply since it is a naturally occurring component in the Earth's atmosphere. Moreover, recent advancements in gas polarization technologies have attained Xe-129 polarization levels approaching 50% with liter output volumes, which allows clinical lung imaging with HP Xe-129 to be feasible [11-12].

1.B.1 Hyperpolarized Xenon-129

Xe-129 has several unique properties that makes it an attractive alternative to He-3 in HP gas imaging. It is extraordinarily sensitive to its chemical environment and is capable of producing an enormous range of chemical shifts [13]. It also has a relatively high solubility in biological tissues and can easily diffuse into the surrounding pulmonary tissue and red blood cells (RBCs). By exploiting these unique properties, regional ventilation and gas uptake-exchange throughout the lungs can be assessed to gain a better understanding of pulmonary physiology and disease progression [14].

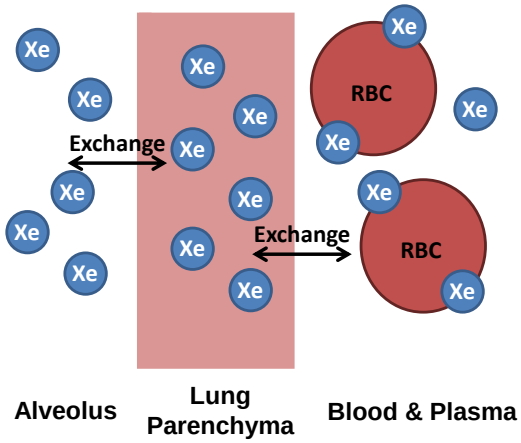

Figure 1: Diagram of the Xe-129 exchange process. After inhalation, a dynamic equilibrium of Xe-129 is established between the alveolar air spaces, lung parenchyma, RBC, and Plasma. The HP Xe-129 atoms first diffuse from the air spaces into the lung parenchyma and then into the RBC and plasma. Adapted from [5].

Following inhalation, the majority of the HP Xe-129 remains in the lung air spaces (Figure 1). Only 1-2% of the Xe-129 is dissolved into the lung parenchyma, plasma, and RBCs, which are collectively termed the “dissolved phase” [15]. There is a dynamic equilibrium between the gaseous and dissolved Xe-129, in which there is a continual exchange of polarized and depolarized xenon atoms. Each compartment (gas, lung parenchyma, plasma, and RBCs) produces a detectable MR spectral peak at a distinct resonant frequency. However, the lung parenchyma and plasma compartments are collectively called the “tissue” compartment because they have similar chemical shifts of 196 parts per million (PPM) relative to the gas peak. Gaseous Xe-129 typically produces a peak with the largest amplitude, and the dissolved phase produces a smaller set of peaks with a chemical shift approximately 200 PPM away from the main gas peak (Figure 2) [16-18].

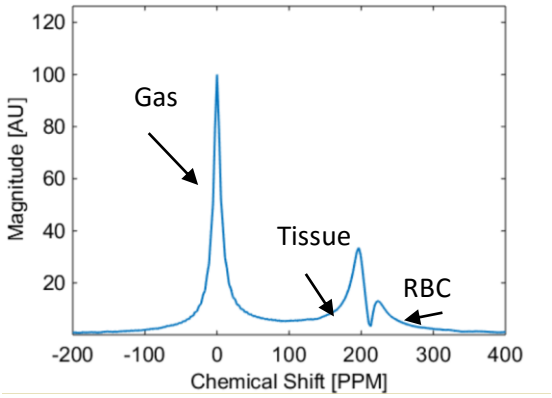

Figure 2: Representative Xe-129 spectrum of healthy human lungs with three main peaks: gas (0 PPM), tissue (196 PPM), and RBC (215 PPM).

1.B.2 Dissolved Phase Imaging

Although only a small fraction of the inhaled xenon enters the dissolved phase, many studies have demonstrated that directly imaging the dissolved phase is feasible. Early studies in 1990 by Swanson et al. imaged the dissolved phase in small animals using chemical shift imaging (CSI) with a multiple-breath inhalation protocol [19]. In 2010, two different research groups were able to demonstrate three-dimensional imaging of the dissolved phase in human subjects within a single breath hold period. However, these techniques were only able to assess the total dissolved phase signal and could not distinguish between the individual tissue and RBC components [20-21]. To overcome this problem, Dixon-based techniques capable of separately imaging each compartment were developed [22-23]. The Dixon imaging technique was originally created for separating signals originating from water and fat in proton MR imaging by taking advantage of their different resonant frequencies.

While these techniques represent important steps in extracting the wealth of information provided in hyperpolarized Xe-129 imaging, they do not fully exploit xenon's extraordinary sensitivity to its chemical environment. There may be other unknown peaks that are seen only in diseased subjects and cannot be detected without acquiring the full chemical shift spectrum. These new peaks can provide novel information for understanding disease progression and evaluating treatment efficacy.

1.C. 3D- Single Breath Chemical Shift Imaging

This work focuses on 3D Single Breath Chemical Shift Imaging, a technique pioneered by the HP gas research group in the Department of Radiology and Medical Imaging at the University of Virginia. 3D-SBCSI uses a combination of MR spectroscopic imaging and hyperpolarized Xe-129 to exploit xenon's ability to dissolve into biological tissue and produce MR spectral peaks with distinct resonant frequencies. This method is capable of non-invasively assessing regional lung ventilation and gas uptake and exchange in 3D within a single breath hold (less than 10 seconds). Earlier work has demonstrated that 3D-SBCSI is capable of detecting regional ventilation defects and changes in gas uptake and exchange [24-28]. Moreover, 3D-SBCSI acquires the full Xe-129 chemical shift spectrum, which can be used to identify previously unknown peaks in diseased subjects.

The 3D-SBCSI pulse sequence is a modified version of the standard CSI pulse sequence that has been adapted to be compatible with hyperpolarized Xe-129. Since this technique is intended for clinical lung imaging, the pulse sequence has been compacted to have an acquisition time on the order of a breath hold.

The signal from the dissolved phase is maximized by applying the radio frequency (RF) pulse at the dissolved phase frequency, approximately +200 ppm from the gas frequency. Unlike proton MR spectroscopy, the longitudinal magnetization of HP Xe-129 does not recover after excitation by an RF pulse. A small flip angle of 25^{o} is applied to efficiently use the finite amount of available signal. Standard CSI pulse sequences typically use flip angles > 30^{o} for greater excitation and better SNR [29]. Using a relatively small flip angle tips less of the magnetization into the transverse plane, which ensures that there is sufficient signal available for the entire duration of the acquisition. Additionally, the repetition time (TR) of the pulse sequence can be minimized since there is no need to wait for signal recovery between RF excitations. A minimum TR of 13.1 ms is used to allow sufficient time for the diffusion and exchange of polarized and unpolarized xenon atoms among the different compartments [16]. Xe-129 in the dissolved phase has a short transverse relaxation time (T2*) on the order of 1.5 to

2.4 ms [30-31]. The shortest possible echo time (TE) of 1.0 ms, and is based on hardware and excitation limitations. The 3D-SBCSI pulse sequence utilizes an elliptical sampling pattern of k-space to further reduce the acquisition time. Elliptical sampling is a widely applied strategy in MR spectroscopy, where the corners of k-space are not sampled to encode an elliptical k-space. Using the elliptical sampling pattern reduces the acquisition time by approximately 50% in comparison to fully sampling the k-space. However, some spatial resolution is lost as a result [32-33].

1.D. Magnetic Resonance Spectroscopy Signal Processing

The signal acquired during an MR spectroscopy study is called the free-induction decay (FID) signal. The acquired FID signal is in the time domain, and then Fourier transformed to obtain the desired spectrum in the frequency domain. Theoretically, there is no difference in the information provided between the two different domains. However, analyzing MR spectroscopy data in the frequency domain is preferred because it allows for easier visual interpretation and quantification of the different chemical species present [34].

The measured FID signal is a complex exponentially decaying time-domain signal. Applying the Fourier transformation to the FID signal results in a spectrum with a complex peak that is characterized by a Lorentzian line shape (Figure 3). The real part of the spectrum shows the peak in the absorption mode, whereas the imaginary part shows it in the dispersion mode [35]. Quantification is typically completed using the real part with the absorption mode since it corresponds to a positive peak with the narrowest width. Using the imaginary part for quantification is undesirable because the peak is wider and contains both positive and negative parts. Closely neighboring peaks in the imaginary part can overlap and cancel each other.

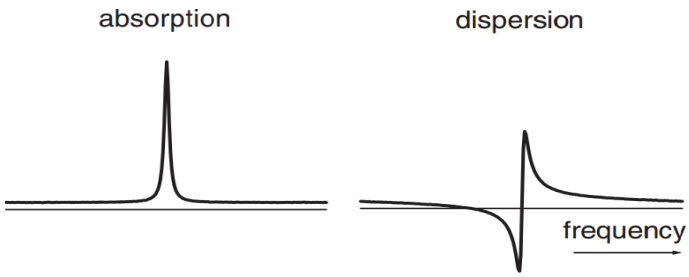

Figure 3: Resulting absorption and dispersion mode Lorentzian line shapes from the Fourier transform of an exponentially decaying time-domain signal. Adapted from [35].

Moreover, the measured FID signal contains an arbitrary phase which results in a spectrum with the real part comprising of a mixture of the absorption and dispersion modes (Figure 4). A constant phase shift is introduced into the FID signal due to the scanner's inability to detect the exact x- and y- components of magnetization. Additionally, there is a frequency dependent phase shift caused by off-resonance effects of the RF pulse. The spectrum can be corrected by multiplying the whole spectrum by a constant zero-order phase correction and a linear frequency dependent first-order phase correction [36]. The spectrum is considered to be "phase corrected" when the real part of the spectrum contains only the absorption mode line shape. In the event phase correction proves to be too difficult, the absolute spectrum can be used, which is phase independent. While the peaks in the absolute spectrum are positive, they are also wider compared to the same peaks in the phased corrected real part.

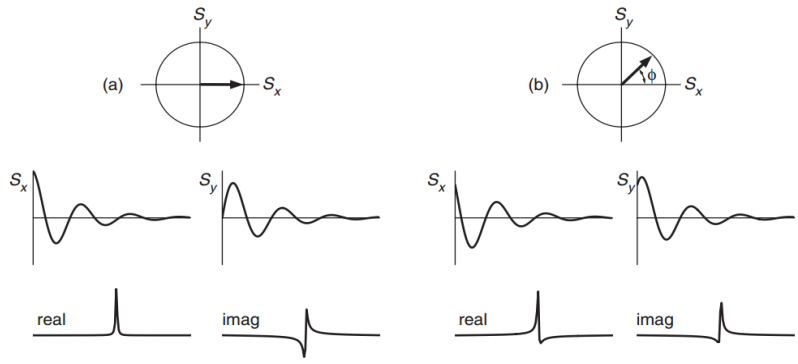

Figure 4: Diagram illustrating the effect of phase shifts on the real and imaginary parts of the spectrum. When a spectrum is de-phased, both the real and imaginary parts contains a mixture of the absorption and dispersion modes. Adapted from [35].

After applying the appropriate phase correction, the real part of the spectrum is typically used to quantify the relative concentrations of each chemical-species. Traditionally, spectroscopic studies use the area integration method, where boundaries for each peak are defined and then integrated. While integration is the most straightforward method for quantification, it faces difficulties in accurately quantifying peaks that are overlapping or have a wavy baseline. An alternative and more robust method for quantification are model line fitting methods using a priori information about the spectrum [37].

An in-depth description of the post-processing tools developed for 3D-SBCSI and a comparison of quantification methods are described in Chapter 2. Clinical work with 3D-SBCSI in interstitial lung disease (ILD) and lung cancer (LC) are presented in Chapter 3. Final concluding remarks and potential future work with 3D-SBCSI are given in Chapter 4.

Chapter 2: Post Processing Xe-129 3D-SBCSI Data

The post processing of Xe-129 3D-SBCSI data was completed with in-house built software termed “Tools for Automated Spectral Processing” (TASP) in MATLAB (Mathworks, Natick, MA). TASP was developed to address the need for a tool that can automate the processing and quantification of Xe-129 MR spectroscopy data. Having an automated tool eliminates the need for manual corrections and quantification steps, thus allowing for more accurate results. TASP includes three different modules: (1) Pre-FT Processing, (2) Post-FT Processing, and (3) data visualization (Figure 5). Each module is elaborated more in-depth in the following sub-sections.

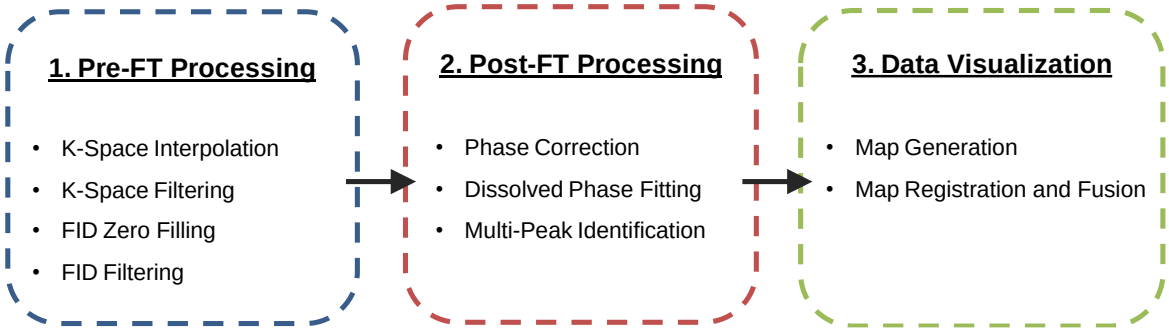

Figure 5: Summary of the three different modules and work flow in TASP.

2.A. Pre-FT Processing

2.A.1 k-space Interpolation and Filtering

Zero filling is used to interpolate the initial k-space matrix of 18x18x6 to 64x64x6 by substituting the unmeasured data points with zeros (Figure 6). Adding zeros into the matrix does not introduce any new information; thus, the image’s actual resolution and SNR does not change. Nevertheless, zero filling the k-space matrix is an effective method for image interpolation. By decreasing the apparent voxel size, the images has a smoother and less pixilated appearance [38-39]. After interpolation, the in-plane k-space matrix is multiplied by a 2-D Gaussian filter to reduce truncation

artifacts. However, the 2-D Gaussian filter also causes the images to appear blurred because the final filtered image is a convolution between the original image and filter. The 2-D Gaussian filter is generated with the MATLAB "*mvnpdf*" function using the parameters: mu = [0, 0] and sigma = [32, 0; 0, 32]. No filtering is applied in the 3rd dimension.

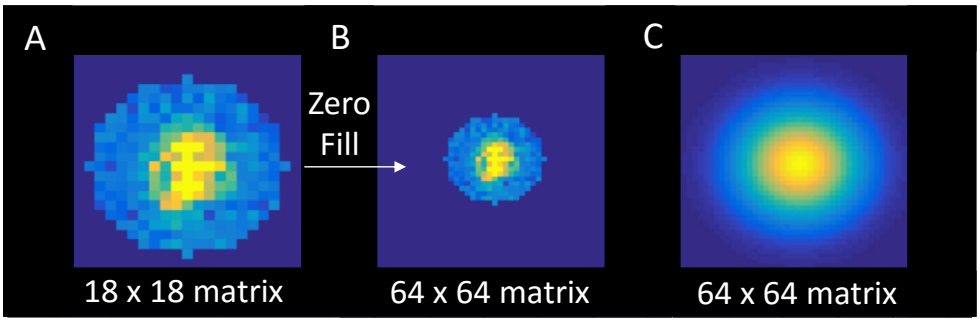

Figure 6: (A) Original 18x18 k-space Matrix acquired with an elliptical sampling pattern. (B) The original matrix A is zero-filled to a produce a zero-filled 64x64 matrix. (C) 2D Gaussian matrix that is multiplied point wise with the zero-filled matrix B.

2.A.2 FID Zero Filling and Filtering

Like the k-space matrix, the FID signal is also zero filled by adding an equal number of zeroes to the end of the original time-domain signal. This operation doubles the number of data points in the FID signal from 512 to 1024 data points, which results in a spectrum that is also doubled from its original length. Zero filling the FID signal does not change the resolution and SNR of the spectrum. However, the line shapes of the peaks are better visually defined due to the increased number of data points representing the peaks.

A typical FID signal is the strongest at the beginning and decays over time with the noise remaining constant throughout the entire signal. This implies that the beginning of the FID signal contains the most information and the end of the signal is dominated by noise. By filtering the signal with a decaying function, the end of the FID signal is attenuated while the earlier parts are not affected as strongly. This improves the SNR of the spectrum, but it also causes the peaks to broaden depending on the characteristics of the applied filter. Several types of Lorentzian and Gaussian filters at

different frequencies were tested. A 50 Hertz Lorentzian filter was chosen because it offered a good balance between SNR improvement and linewidth broadening.

2.B. Post-FT Processing

2.B.1 Automatic Phase Correction

By convention, a spectrum is defined to be “phase corrected” when all of the peaks in the real part are in the absorption mode. These corrections are often manually completed by trial and error, so results derived from the same set of spectra can vary between different spectroscopists [35]. This introduces an unknown spectroscopist-dependent error that is difficult to account for when interpreting results from multiple sources. To address this issue, TASP uses an automated phase correction algorithm that was developed for HP Xe-129 spectroscopy.

Traditionally, constant “zero order” and linear frequency dependent “first order” corrections are used to phase correct the spectrum. With the peaks in the absorption mode, the chemical species are quantified by integrating the area under each peak. However, in the phase correction step of TASP, only a zero order correction is applied. A first order correction is not needed because TASP uses a model line fitting method that does not require the spectrum to be fully phase corrected before quantification. A zero order correction is also theoretically not required but is included because it improves the overall computational efficiency of the model line fitting method. By phase correcting the gas peak with a zero order correction, the tissue and RBC peaks have a similar relative phase shift and line shape from voxel to voxel. This improves the computational efficiency of the fitting algorithm because information from fitting one voxel can be used to fit a subsequent one. The zero order correction is determined iteratively by finding a solution that maximizes the integral of the gas peak (Figure 7). The gas peak is better suited for finding the appropriate zero order correction since it is a single peak that does not overlap with any other neighboring peaks.

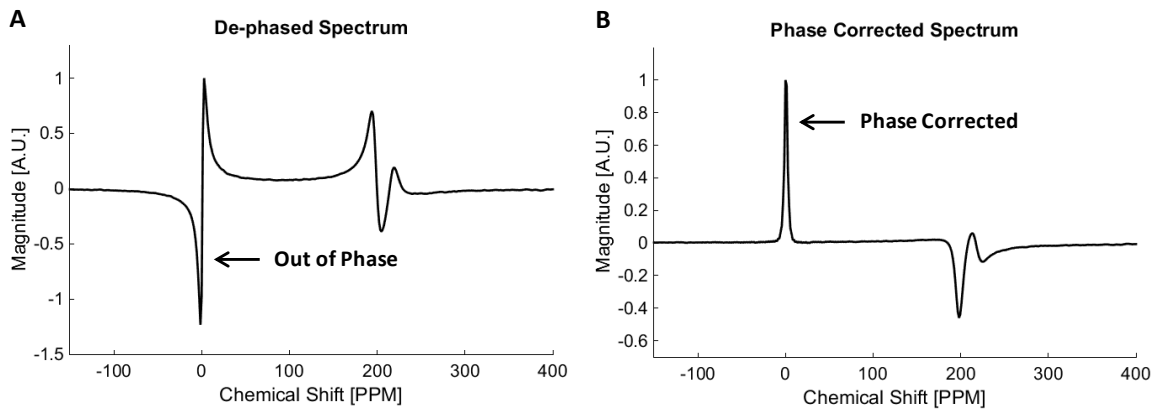

Figure 7: (A) Initial de-phased Xe-129 spectrum with the gas peak out of phase in the dispersion mode. (B) Resultant phased corrected spectrum with the gas peak in the desired absorption mode. The tissue and RBC peak were not phase corrected.

2.B.2 Dissolved Phase Fitting

TASP uses a model line fitting method to quantify the gas, tissue, and RBC peaks in a given Xe-129 spectrum. Each peak is fitted according to a Lorentzian model as described in equations (1) and (2) [31]. The Lorentzian model accounts for four different parameters including the amplitude, width, center frequency, and phase. By default, TASP only fits the known gas, tissue, and RBC components for all voxels. However, it is simple to adapt TASP to fit any number of peaks given that there is sufficient SNR to obtain a reliable fitting. With the default settings, TASP solves for 12 different variables iteratively by minimizing the sum of the absolute differences between the fittings and data.

$$(1) \qquad Re[F(f)] = \frac{A_c(w_c \cos\theta_c - (f - f_c)\sin\theta_c)}{(f - f_c)^2 + w_c^2}$$

$$(2) \qquad Im[F(f)] = \frac{A_c(w_c \sin\theta_c + (f - f_c)\cos\theta_c)}{(f - f_c)^2 + w_c^2}$$

$$A = amplitude; \quad w = width; f_c = center\ frequency; \quad \theta_c = phase$$

Traditionally, only the real part of the spectrum is used for quantification; however, in TASP both the real and imaginary parts of the spectrum are simultaneously fitted. This is essential in developing a robust model fitting method because when there are overlapping peaks, as there are in Xe-129 3D-SBCSI, a unique solution to the fitting problem often does not exist. Using both parts of the spectrum constrains the number of possible solutions, which improves the solver's ability to consistently converge on to meaningful solutions. To further constrain the solution space, the solver also uses a priori information of the spectrum provided by the user. For each component, the user defines an initial value and boundaries for each parameter. The peak positions and T2* values are chosen based on literature values, while the amplitude and phase are chosen based on results from simulations.

The user defines initial values and boundaries for each of the parameters to be fitted (Figure 8). The initial values and boundaries used are summarized in Table 1.

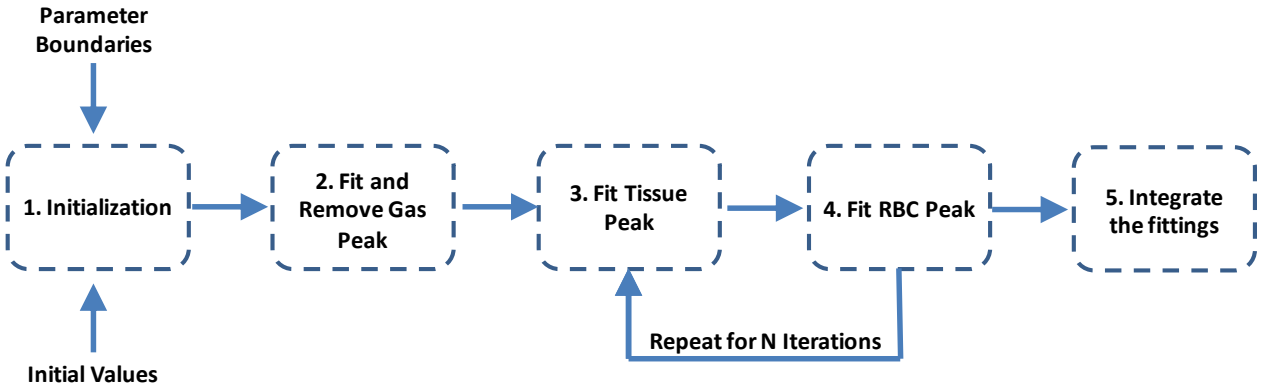

Figure 8: Process work flow diagram of the dissolved phase fitting algorithm in TASP.

Fitting the spectrum is in an iterative process, in which the program progressively minimizes the error and calculates an R^2 value between the fittings and the data at each iteration. This process continues until a maximum number of 1000 iterations is reached or an R^2 value of 0.98 is obtained. The program first fits the gas peak and subtracts it from the original data, resulting in a spectrum with only the tissue and RBC peaks. Next, the program attempts to fit the tissue peak and then the RBC peak until the termination conditions are reached. For the peak that is currently being fitted, all other peaks are

simulated and subtracted from the spectrum using either the initial conditions or fitted parameters from a previous iteration. The resulting subtracted spectrum is used to solve for the parameters of the peak being fitted. Figure 9 shows example fittings for the real, imaginary, and absolute components of a representative Xe-129 spectrum from a healthy subject. The Lorentzian model was able to fit the data well with a $R^2 > 0.98$.

Table 1: Initial values and boundaries for fitted parameters.

Parameters	**Gas Peak**		**Tissue Peak**		**RBC Peak**	
	Initial Value	Boundary	Initial Value	Boundary	Initial Value	Boundary
Center [PPM]	0	-25 – 25	196	194 – 200	215	212 – 221
Phase [Degrees]	360	340 -380	340	300 – 380	260	220 – 300
Width [ms]	10	0 – 25	2.3	1.8 – 2.6	1.8	1.2 – 2.6
Amplitude [A.U.]	100	0 – inf.	3	0 – inf.	1	0 – inf.

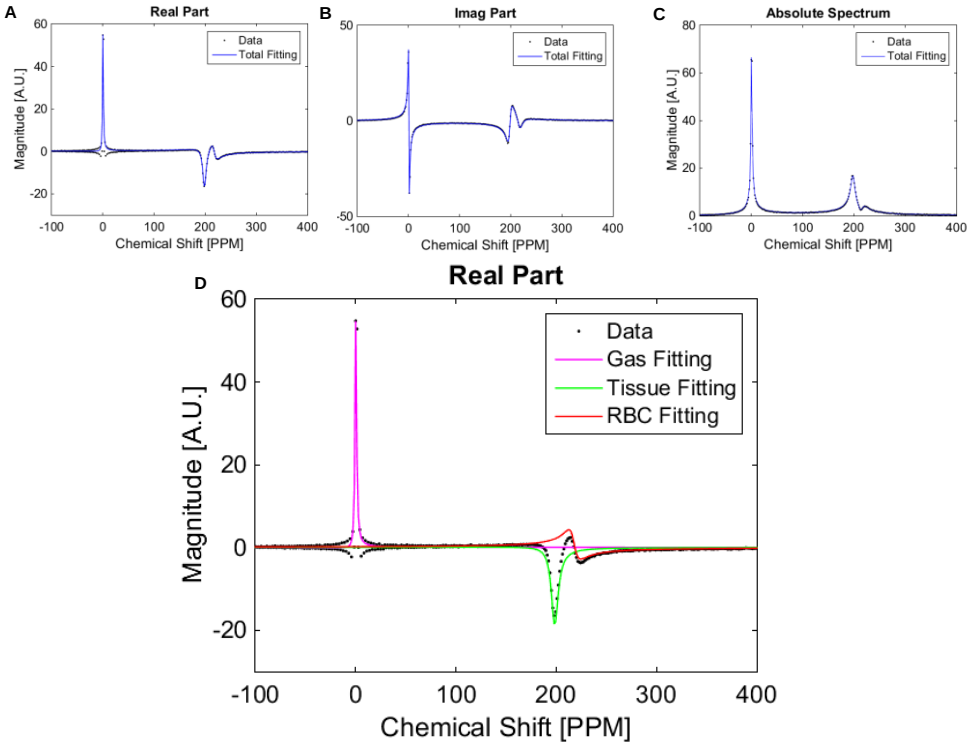

Figure 9: Fittings of the (A) Real Part, (B) imaginary part, and (C) absolute spectrum are superimposed upon their respective parts of the original data. The total fitting is the sum of the individual gas, tissue, and RBC fittings (D) Fitted real part of a representative Xe-129 spectrum from a healthy subject with the individual fittings shown for each component. The total fitting for the real, imaginary, and absolute spectrum typically have a $R^2 > 0.98$.

2.B.3 Multi-Peak Detection

In addition to the gas and dissolved phase peaks, there may be other unknown peaks in diseased subjects that have yet to be identified. Xenon is capable of producing an enormous range of chemical shifts in response to its chemical environment. New peaks may arise as a result of the xenon interacting with the abnormal chemical environment caused by the disease. In 3D-SBCSI, the full Xe-129 chemical shift spectrum for each voxel is acquired, which can be used to identify new peaks without a priori information.

Assuming that the spectrum has sufficient spectral resolution and SNR, there are two other confounding factors that can mask the new peak's existence within a spectrum. The first is that the new peak may be overlapping and hidden within the tails of neighboring peaks. The second is that the new peak may be out of phase. This results in the new peak having a reduced amplitude and wider peak shape, which may prevent its detection. To address these issues, the fittings of the known Xe-129 peaks are subtracted from the original spectrum, which results in a difference spectrum that is ideally comprised of signal only from the new peaks and noise. The absolute component of the difference spectrum is used in all subsequent steps because the absolute component is phase independent, in which all of the peaks have the ideal absorption mode line shape. To distinguish potentially new peaks from the noise, an amplitude threshold based on the statistics of the noise as seen in equation (3) is used. The *"a"* constant by default is set to 4, but it can be changed by the user to change the threshold to the desired level.

Having a low threshold results in many false positive identifications, while a high threshold may fail to identify new peaks with a lower amplitude.

$$(3) \quad Threshold = \mu_{noise} + a * \delta_{noise}$$

$$\mu = mean; \;\; a = constant; \;\; \delta = standard\ deviation$$

In practice, the difference spectrum contains residual signals from the gas or dissolved phase peak because the fittings are not perfect. Depending on the accuracy of the fittings, the residual signals can cause false positive errors. The user should visually review the spectra flagged by the multi-peak detection algorithm to validate the results (Figure 10).

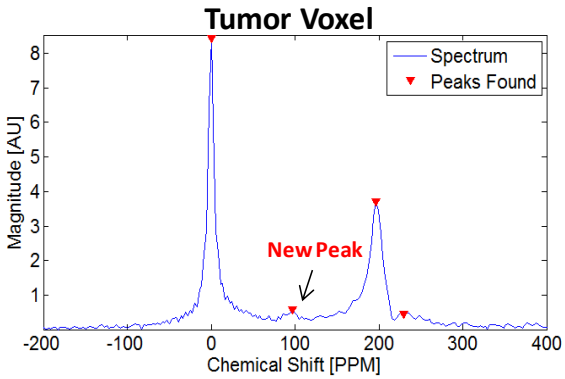

Figure 10: Spectrum of voxel from the location of a tumor in subject LC1. Peaks identified by the algorithm are marked by red triangles pointing towards the location of the peak. A peak corresponding to the presence of a tumor was identified at 97 PPM in the spectrum.

2.C. Data Visualization

2.C.1 Map Generation

After completing the fitting process, the estimated parameters of each component are used to calculate its peak area, T2*, and peak position relative to the gas peak. The area of each component's peak cannot be directly compared between different 3D-SBCSI acquisitions because it is dependent not only on the physiological changes in the lung but also the inhaled HP Xe-129 volume and polarization level. To have comparable measurements independent of polarization levels, the Tissue/RBC, Tissue/Gas, and RBC/Gas ratios are calculated (Figure 11). The Tissue/Gas and RBC/Gas ratios describe the fraction of gaseous xenon dissolved into the tissue and RBCs. On other hand, the Tissue/RBC ratio represents the exchange of xenon between the tissue and RBCs.

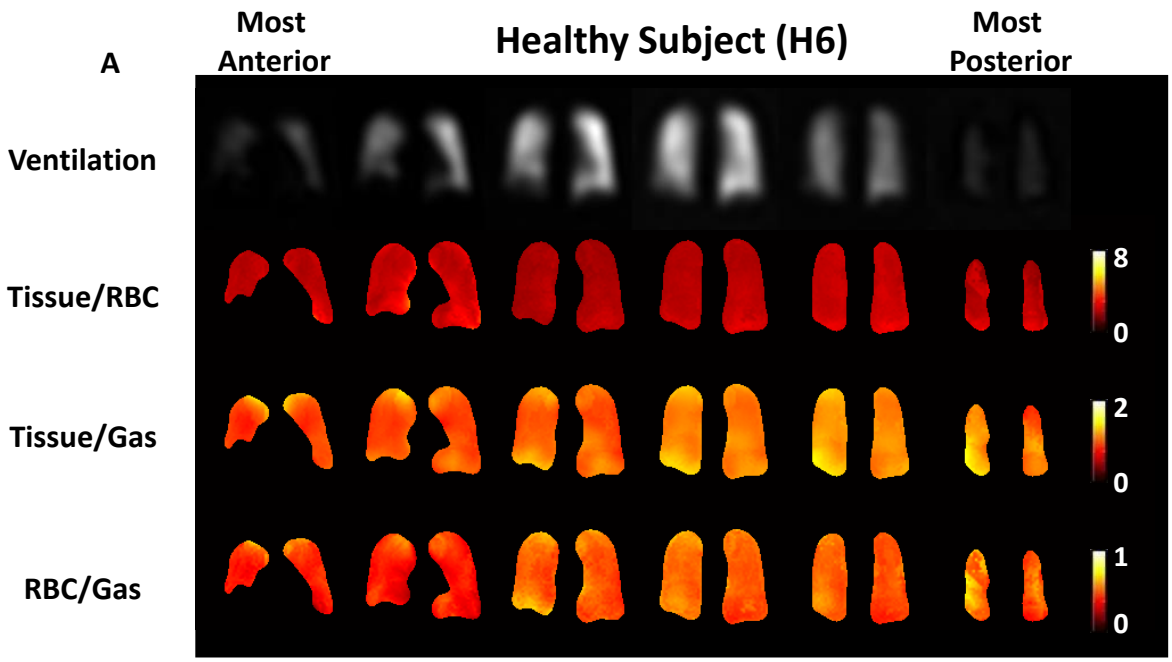

Figure 11: Coronal 3D-SBCSI maps of Xe-129 ventilation, Tissue/RBC, Tissue/Gas, and RBC/Gas ratio maps in a representative healthy subject, H6.

The gas, tissue, and RBC maps are interpolated from an in-plane matrix of 64x64 to 128x128 using the bicubic interpolation method. The interpolated values are calculated based on the weighted average of the nearest 4x4 voxel neighborhood. After interpolation, Tissue/RBC, Tissue/Gas, and RBC/Gas maps are calculated using the appropriate gas, tissue, and RBC maps.

After interpolation, a two-tiered threshold mask is applied to the maps so that only voxels corresponding to the lungs are quantified. A simple threshold is not used because there are some ringing artifacts due to under sampling that have a signal intensity comparable to that of the edges of the lung in the most anterior slices. Applying a simple threshold can remove these artifacts, but the edges of the lungs are also removed.

For this reason, a two-tiered threshold is used to remove the artifacts and preserve the edges of the lungs. A high-value threshold is first applied to remove the noise, artifacts, and the edges of the lungs. The remaining voxels are called the seed region. Voxels adjacent to the seed region are then compared to the lower threshold. If

the signal intensity of an adjacent voxel is greater than the lower threshold, it is added back into the map (Figure 12). This process continues and the seed region grows until there are no more adjacent voxels that has a greater signal intensity than that of the lower threshold. By performing a two-tiered threshold, the edges of the lungs are initially removed, but are then recovered by growing the seed region iteratively.

The high and low thresholds of the mask are chosen based on the level of noise in the image. The mean and standard deviation of the noise is estimated from voxels that should have no signal, such as first and last rows in an image. The thresholds are calculated according to equation (3). For this mask procedure, the user selects a high and low value for the threshold., If the high threshold is too large, then only one or none of the lungs appear in the initial seed region. However, if the high threshold is too small, then noise is included in the final mask. On the other hand, the lower threshold needs to define to be large enough so that the final mask does not include noise. However, if it is too large then the edges of the lungs are removed from the mask.

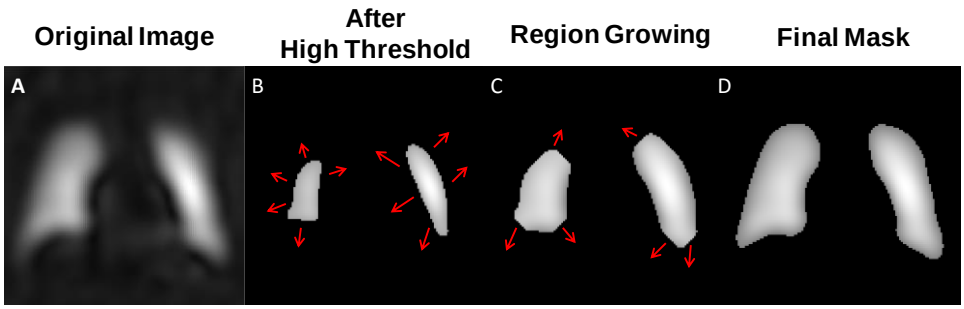

Figure 12: The high-value threshold is applied to the original image (A) to produce two seed regions at the center of each lung (B). These seed regions undergo an iterative region growing process and expands towards the edges of the lungs (C). The final mask is obtained when there are no more voxels adjacent to the mask that meet the lower threshold criteria (D). Red arrows denote the general direction of region growing.

2.C.2 Map Registration and Fusion

In addition to the 3D-SBCSI acquisition, a set of matching proton images are also acquired within the same breath hold. This allows for the proton images to be easily registered with the 3D-SBCSI maps without having to correct for potentially different lung inflation levels (Figure 13). The proton images are used in conjunction with the 3D-SBCSI maps to identify abnormalities in the lungs such as ventilation defects. TASP automatically performs the registration using MATLAB's intensity-based image registration function.

Due to the difference in resolution and slight variations in the lung inflation level, the CSI ventilation image does not perfectly register with the protons. Certain areas at the bottom of the lungs or near the heart in the proton images that should not be ventilating are mismatched with the CSI ventilation image. The slice thickness of the CSI images is greater than that of the protons; thus, there are volume averaging effects seen in the CSI ventilation images.

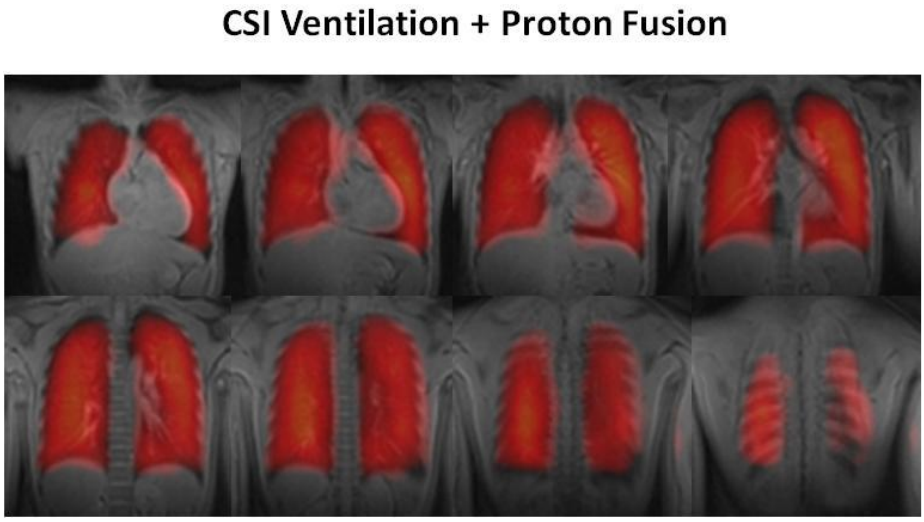

Figure 13: Fusion images of the 3D-SBCSI ventilation image with matching protons of a representative healthy subject, H5.

2.D. Quantification Method Comparison

Prior to the development of TASP, post processing was completed using 3DiCSI (Qi Zhao, Columbia University, NY), an interactive software package that allowed for the manipulation and processing of CSI data. However, the only quantification method supported in 3DiCSI was the area integration method. This method is the most straight-forward and computationally inexpensive method for quantifying MR spectral data. However, it is difficult to reliably apply this method to biological MR spectral data due to the presence of wavy baselines, poor SNR, and extreme overlap of neighboring peaks. The most prevalent issue in HP Xe-129 spectral data was the overlap between the tissue and RBC peaks. To overcome this problem, a Lorentzian line fitting method was used to separate and quantify the peaks. In this section, these two methods were compared in terms of their accuracy in quantifying the Tissue/RBC ratio in simulated spectra (Table 2). Simulation parameters for each peak (amplitude, width, center frequency, and phase) were based on the average fitted parameters of all spectra from a healthy subject, H6. These parameters were kept constant for all simulations when appropriate. The gas peak was not included in the simulations since it would be trivial to fit and remove from the spectrum prior to quantifying the tissue and RBC peaks with either method.

Table 2: Pros/Cons of the Area Integration and Fitting Quantification Methods

	Area Integration	**Dissolved Phase Fitting**
Pros (+)	• Computationally inexpensive. • Straightforward and intuitive.	• Separates overlapping peaks and quantifies each peak individually. • Accounts for changes in the phase, center frequency, and peak width.
Cons (-)	• Difficult to separate overlapping peaks. • Assumes spectrum is phase corrected.	• Computationally expensive. • Requires prior knowledge of the spectrum.

Theoretically, as the separation between the tissue and RBC peaks increases, the error of the area integration method should decrease. To test this hypothesis, simulated spectra with the RBC peak shifting between -20 to 100 ppm from its original peak position were quantified (Figure 14A). At a shift of -20 ppm, the tissue and RBC peak were completely overlapped and cannot be distinguished.

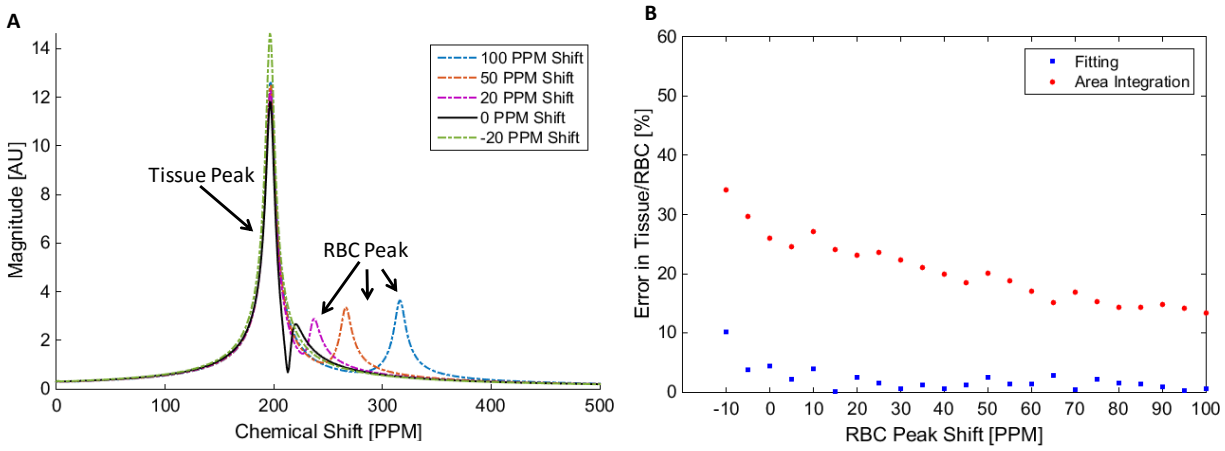

Figure 14: (A) Simulated spectra with the RBC peak shifting -20 to 100 PPM relative to its original peak position at 197 PPM. A positive peak shift meant the RBC peak moved away from the tissue peak. The RBC peak became separated from the tissue peak as the RBC peak shift increased. (B) Error in the Tissue/RBC ratio using the fitting and area integration method for different simulated RBC peak shifts. Simulation parameters were chosen for a Tissue/RBC value of 2.6.

The error of the integration method increased when the RBC peak was shifted towards the tissue peak and decreased when the RBC peak was shifted away from the tissue peak (Figure 14B). The error did not reach 0% after a shift of 100 ppm because the tails of the tissue and RBC peaks were still overlapping. The decrease in the error appeared to follow an exponential decay. This occurred because shifting the RBC peak away from the tissue peak provided diminishing returns on the amount of separation achieved. For a physiological relevant range of RBC peak shifts (-5 to 5 PPM), the average error of the area integration method was ~27%. On the other hand, the fitting method had a much lower average error of ~3% for a physiological relevant range of RBC peak shifts.

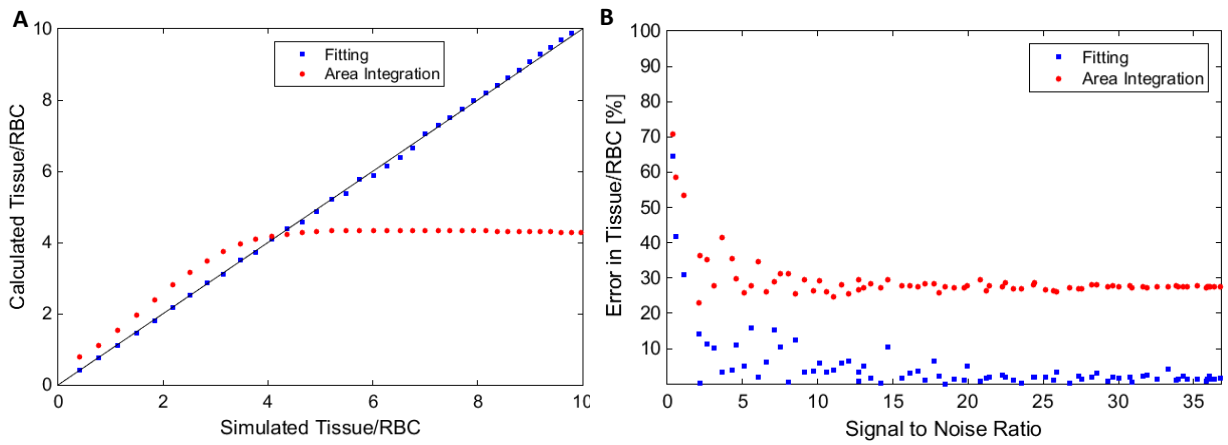

Figure 15: (A) Comparison of the calculated Tissue/RBC ratios using fitting and area integration methods versus the simulated ratio values. The ratio values were varied by changing the tissue peak amplitude in the simulations. The black line represents an ideal method, where the simulated ratio value were perfectly quantified. (B) Error in the Tissue/RBC ratio for simulated spectra with varying SNR using the fitting and area integration methods. Simulation parameters were chosen for a Tissue/RBC value of 2.6.

In addition to the RBC peak shifts, each method was also tested for their accuracy in quantifying the Tissue/RBC ratio over a range of simulated ratio values and SNR (Figure 15A). The area integration method did not reliably quantify the ratio value for simulated ratio values ≥ 4. As the simulated ratio increased, the tissue peak became more overlapped with the RBC peak. The area integration method was not able to distinguish between the two peaks and was overestimating the RBC peak area at simulated ratio values ≥ 4. The fitting method was more robust compared to the area integration method. It was capable of correctly quantifying the ratio value over the full simulated range with an average error of ~3%. The error of the fitting method does appear to be slightly larger at higher simulated ratio values due to the increased overlap between the tissue and RBC peaks.

Finally, varying levels of noise were added to the same simulated spectrum to determine the effect of noise on the accuracy of the quantification methods (Figure15B). As the SNR increased, the error in quantifying the Tissue/RBC ratio also decreased for both methods. A typical spectrum from actual data has an SNR > 40 in healthy subjects and SNR > 21 in diseased subjects. Based on these simulations, it was anticipated that

the error of the area integration method is ~27% while the error for the fitting method is ~3% for actual data of both healthy and diseased subjects.

In summary, we presented TASP, a MATLAB based software package for the automatic post-processing of HP Xe-129 3D-SBCSI data. TASP is comprised of three components including, Pre-FT processing, Post-FT processing, and Data Visualization (Figure 5). In the Pre-FT processing step, the k-space matrix is interpolated from 18x18x6 to 64x64x6 via zero filling of the k-space. A 2-D Gaussian was applied to the in-plane dimensions of the k-space, and no filter was applied to the third dimension (Figure 6). The FID is also zero filled from 512 to 1024 data points and a 50 Hz Lorentzian filter was applied to the FID.

In the Post-FT processing step, a zero order phase correction is applied and the spectra is fitted to a Lorentzian model accounting for peak phase, center frequency, width, and amplitude. After defining initial values and boundaries for each fitted parameter, the software iteratively solves for each one until a maximum number of 1000 iterations is reached or a $R^2 > 0.98$ is obtained (Figure 9). After fitting the known gas, tissue, and RBC peaks, TASP attempts to find other peaks in the spectra that are above a user defined noise threshold.

In the final Data Visualization step, a mask of the lungs is generated using a two-tiered thresholding process so that only voxels corresponding to the lungs are included in the analysis. With this mask, Tissue/RBC, Tissue/Gas, and RBC/Gas ratios are generated for each subject (Figure 11)The 3D-SBCSI maps are fused with a matching set of proton images that are acquired during the same breathhold as the 3D-SBCSI sequence (Figure 12).

To compare the accuracy and robustness of each quantification method, three different simulations were performed including: shifting the RBC peak, varying the simulated Tissue/RBC ratio, and varying the SNR of the spectrum. The area integration method was less accurate in quantifying the Tissue/RBC ratio in all simulations (Figure 14). This method relied on the user to define appropriate integration widths for each peak in order to quantify the tissue and RBC compartments separately. However, when

there was significant overlap between peaks, it was not possible to define the widths in a way that allowed for each peak to be separately and accurately quantified. On the other hand, the fitting method was able to fit and individually quantify the tissue and RBC peaks. This allowed for a more accurate and reliable quantification of the Tissue/RBC ratio over a range of simulated ratio values and SNR (Figure 15). The fitting method had an average error of approximately 3% in quantifying the Tissue/RBC ratio. For this reason, the fitting method was the preferred quantification method and was used for the post processing of 3D CSI data.

Chapter 3: Clinical Work with 3D-CSI

3.A. Methods and Materials

3.A.1 Imaging and Polarization Protocols

All subjects were imaged on a 1.5T clinical MRI scanner (Avanto, Siemens Medical Solutions, USA). Each scanner was equipped with a flexible vest-shaped chest RF coil tuned to the Xe-129 resonant frequency (Clinical MR Solutions, WI). Each subject was positioned supine on the MR table with the RF coil strapped around their chest. A set of 3D proton scout images were obtained to confirm that the lungs were positioned at the isocenter of the scanner. After the position was confirmed, the subject was administered a test dose of natural abundance xenon (26%) and monitored for any potential adverse reactions. All subjects tolerated the xenon well and did not experience any adverse reactions. For all Xe-129 MRI acquisitions, the subject inhaled a gaseous mixture containing 0.75 – 1 liter of hp Xe-129 that was diluted with nitrogen to have a total volume equal to 1/3 of the subject's forced vital capacity (FVC). Immediately following the full inhalation of the gas, the subject was asked to hold his or her breath for the duration of the acquisition. Isotopically enriched (~87%) Xe-129 was polarized to ~35-50% using a commercial prototype system (XeMed LLC, NH). The parameters for the 3D-SBCSI sequence were TR/TE: 13.1/1.0 ms, matrix: 18x18x8 interpolated to 32x32x8, FOV: 280-320 mm^2, and slice thickness: 25 mm.

3.A.2 Subject Information

This study was completed with an IRB approved protocol. Informal written consent was obtained from all participating subjects. Imaging was performed under an investigational new drug application.

For this study, a total of 17 subjects (6 healthy, 8 ILD, 3 lung cancer) underwent 3D-SBCSI. A baseline spirometry examination was performed on all subjects prior to

imaging. All healthy subjects had a Forced Expiratory Volume in 1 second (FEV1) predicted ≥ 90% and FEV1/FVC ≥ 0.78. All ILD subjects had a FEV1 predicted ≤ 90% and FEV1/FVC ≥ 0.75. Subject LC1 was imaged a total four times at 1, 3, 6, and 12 months after receiving radiation treatment.

Table 3: Subject Data for 6 healthy, 8 ILD, and 3 LC subjects.

Subject No.	Category	Sex	FEV1 Pred. [%]	FEV1/FVC	Age (years)
H1	Healthy	F	96	0.87	22
H2	Healthy	F	103	0.81	26
H3	Healthy	F	101	0.95	24
H4	Healthy	F	108	0.99	52
H5	Healthy	F	93	0.84	21
H6	Healthy	M	103	0.78	20
I1	ILD	M	84	0.83	70
I2	ILD	M	80	0.84	73
I3	ILD	M	73	0.76	67
I4	ILD	M	72	0.75	80
I5	ILD	F	32	0.86	38
I6	ILD	F	58	0.83	79
I7	ILD	M	76	0.76	68
I8	ILD	M	73	0.78	56
LC1	Lung Cancer	M	96	0.41	51
LC2	Lung Cancer	M	108	0.81	63
LC3	Lung Cancer	M	90	0.34	61

3.A.3 Post-Processing of 3D-SBCSI Data

Post-processing of all 3D-SBCSI was completed offline using the TASP software package on MATLAB as described in Chapter 2. The original data was interpolated from a matrix of 18x18x6 voxels to 64x64x6 voxels via zero filling of the k-space. The maps generated were later interpolated further from 64x64x6 to 128x128x6 with a bicubic interpolation method. The FIDs were zero filled from 512 to 1024 data points, and a 50 Hz Lorentzian filter was applied. The gas, tissue, and RBC peaks were fitted to a Lorentzian model, and then individually quantified using the respective fittings. A two-tiered threshold mask, as described in sub-chapter 2.C.1,was used to determine all of the relevant voxels located in the lungs.

Ventilation, Tissue/Gas, RBC/Gas, and Tissue/RBC maps were generated on a slice by slice basis for each subject. Whole lung mean and standard deviations, using all voxels within the mask, were calculated for each ratio map. Similarly, the whole lung mean and standard deviation for T_2*, as well asthe individual peak positions were calculated for the tissue and RBC components, and compared to literature values. The mean Tissue/RBC value and standard error was also calculated for each individual slice. Comparison of the whole lung mean Tissue/RBC vs. FVC, RBC/Gas vs. Hematocrit, and differences in the mean Tissue/RBC for healthy and ILD subjects were generated. Hematocrits for six ILD subjects were also acquired. .

The multi-peak detection algorithm was performed on all 3D-SBCSI data to identify any potentially new peaks above a set noise threshold. If a new peak was found, it was quantified by subtracting the gas, tissue, and RBC signal from the spectrum using the individual fittings for each compartment. The new peak was then quantified by defining appropriate boundaries and integrating the spectrum. Area integration was used for this step since all overlapping peaks were removed. After integration, the 3D-SBCSI map of the new peak was normalized by the gas map to account for the fact that the distribution of Xe-129 was not equal throughout the lungs. Finally, the mean and standard deviation of the noise in a given voxel, as described in equation (3), was used to determine whether the new peak had sufficient SNR. For each newly detected peak, three different 3D-SBCSI maps were generated with thresholds of 1, 3, and 5 times the standard deviation of the noise. In order to better visualize the 3D-SBCSI map of the new peak, it was fused with a matching proton image acquired within the same breathhold.

3.A.4 Statistical Analysis

A non-parametric Mann-Whitney U-Test was used to determine if there was a statistically significant difference between the whole lung mean Tissue/Gas, RBC/Gas, Tissue/RBC, and mean Tissue/RBC for each slice between healthy and ILD subjects. The underlying distribution of ratio values for both populations was unknown, thus, a

two tailed t-test cannot be used. Furthermore, each population had a relatively small number of subjects. For these reasons, the Mann-Whitney U-Test was chosen for this analysis [40-41].

3.B. Interstitial Lung Disease

3.B.1 Introduction of Interstitial Lung Disease

Interstitial lung disease (ILD) is a group of pulmonary disorders that predominantly affect the pulmonary interstitium. While there are more than 100 disorders within this group, the most common ones are idiopathic pulmonary fibrosis (IPF), hypersensitivity pneumonitis, sarcoidosis, and connective tissue disease. These disorders are characterized by inflammation and fibrosis of the interstitium leading to progressively reduced lung compliance and impaired gas exchange between the alveoli and capillaries. Exposure to asbestos, toxic drugs, and radiation are some of the identified factors causing ILD. However, the majority of clinical ILD cases have an unknown cause and are largely classified as IPF [42]. The survival rate and treatment options for patients with ILD depend on the underlying disorder. Those with IPF have a median survival of less than three years following diagnosis due to the rapid decline in lung function and lack of effective treatment options. [43-44]. There are some medications under investigation such as Pirfenidone, which can slow but not reverse the disease progression [45-46].

Distinguishing between the many types of ILDs can be challenging because they tend to have similar symptoms and clinical features such as dyspnea and nonproductive coughing. Pulmonary functions tests (PFTs) reveal that most ILDs result in a reduced FVC, FEV1, and lung diffusing capacity for carbon monoxide (D_LCO). While PFTs are able to monitor the loss in lung function, they cannot distinguish which disorder is causing the loss. On the other hand, high resolution computed tomography (HRCT) is able to detect significant radiographic and structural differences between each disorder. HRCT images in IPF reveal a distorted lung architecture and the presence of

honeycombing – a pattern of fibrotic tissue that develops on the periphery of the lungs. More invasive techniques such as bronchoscopy and surgical biopsies can be used to confirm the diagnosis [47-48].

While HRCT provides important structural information, it provides no functional information about the lungs. Furthermore, the patient is exposed to a high dose of ionizing radiation, and can only be imaged with HRCT in 1-2 year intervals for safety reasons. Young children are particularly sensitive to the damaging properties of ionizing radiation and have increased lifetime cancer mortality risks when exposed to radiation. Therefore, HRCT is not suitable for monitoring disease in pediatric populations or disease progression over short time intervals [49-51].

HP Xe-129 MR imaging is a promising imaging modality that overcomes many of the present weaknesses and limitations of PFTs and HRCT. It allows for high-resolution imaging that probes regional lung function and structure without the need for repeated exposure to ionizing radiation. This technique is suitable for use in pediatric populations and monitoring disease progression over short time intervals [21-23]. HP Xe-129 3D-SBCSI is capable of probing regional lung ventilation and gas uptake and exchange between the lung tissue and RBCs. Having this regional information of the lungs may allow for a better understanding of disease progression.

3.B.2 Results for Healthy vs. ILD Subjects

Healthy subjects typically showed a uniform distribution of gas signal intensities and Tissue/RBC ratios throughout the lungs (Figure 16A). The lungs were well ventilated with no ventilation defects and had a homogenous gas uptake and exchange. Furthermore, a gradient from the anterior towards the posterior coronal slices of the lungs was observed in the distribution of gas signal intensities, Tissue/Gas, and RBC/gas ratio maps. This observation was consistent with previous reports of gravity dependent gradient effects when subjects are in the supine position [52-53]. Mean values for the different ratios, chemical shifts, and T2* are summarized in Table 2.

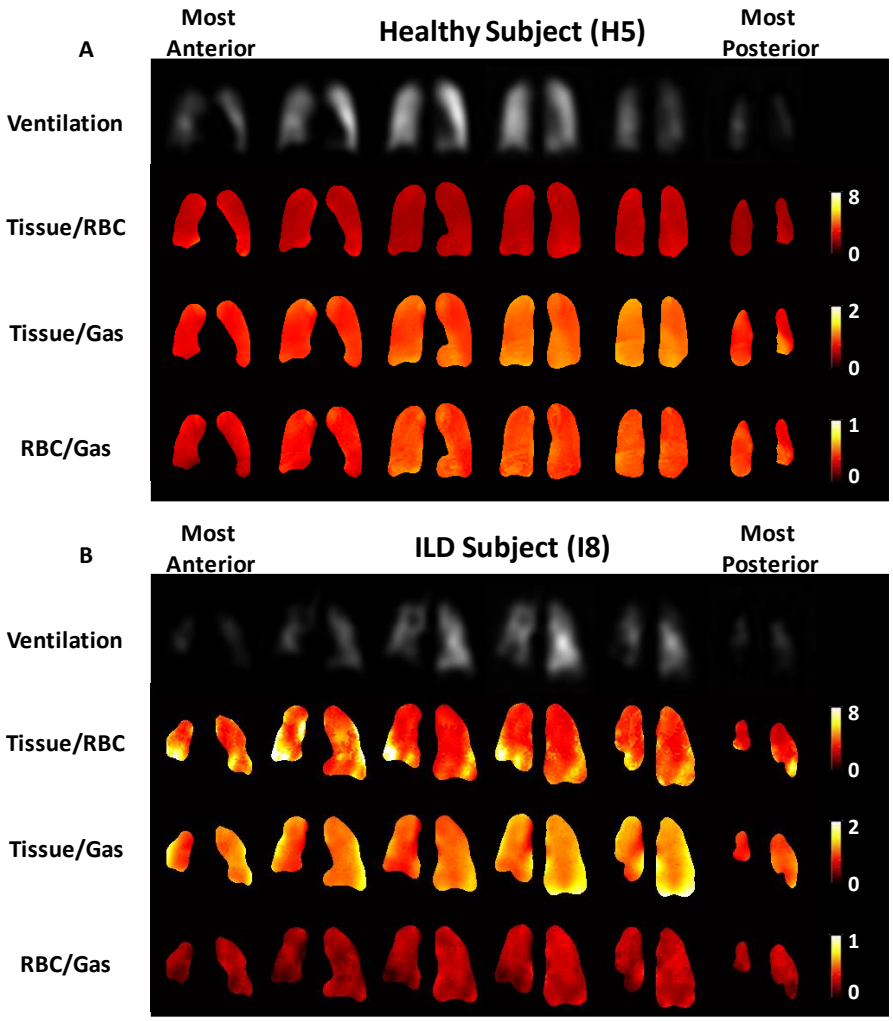

Figure 16: Coronal 3D-SBCSI maps of Xe-129 ventilation, Tissue/RBC, Tissue/ Gas, and RBC/Gas ratio maps in a representative healthy subject, H5 (A) and ILD subject,I8 (B).

Table 4: Summary whole lung mean values for healthy and ILD subjects.

	Healthy	ILD	Healthy Literature [1.C.8]
Tissue to RBC	2.4 ± 0.42	4.9 ± 1.36	-
Tissue to Gas	1.0 ± 0.14	1.2 ± 0.16	-
RBC to Gas	0.4 ± 0.07	0.3 ± 0.11	-
Tissue T_2^* [ms]	2.1 ± 0.06	2.2 ± 0.12	2.3 ± 0.20
Tissue Chemical Shift [PPM]	196.4 ± 0.53	197.5 ± 0.53	197.3 ± 0.60
RBC T_2^*[ms]	1.9 ± 0.04	1.9 ± 0.04	1.7 ± 0.10
RBC Chemical Shift [PPM]	214.9 ± 0.90	215.5 ± 0.76	216.5 ± 1.30

Unlike healthy subjects, those with ILD showed a heterogeneous distribution of gas signal intensities and Tissue/RBC ratios throughout the lungs (Figure 16B). Several ventilation defects were observed, which were likely caused by fibrosis and bronchiectasis. Moreover, there were several regions with high Tissue/RBC ratios predominantly at the periphery and base of the lungs. A high Tissue/RBC ratio indicated that a relatively small fraction of the HP Xe-129 was transferred into the RBCs due to impaired gas transfer. The poor gas transfer between the two compartments was likely to be a result of the interstitium fibrosis. The periphery of the lungs tended to have an increased Tissue/Gas ratio, which was possibly caused by unusually thick tissue and cystic spaces associated with honeycombing.

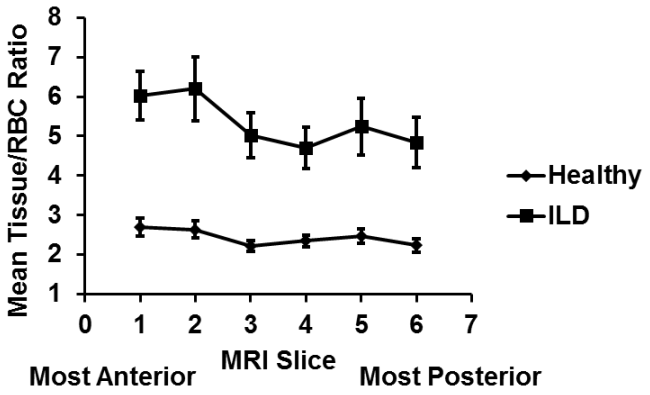

Figure 17: Mean Tissue/RBC of each slice for healthy and ILD subjects. There is a significant statistically difference in the mean Tissue/RBC ratio between healthy and ILD subjects for all MRI slices ($p < 0.05$). Error bars represent the standard error.

Overall, the HP Xe-129 gas uptake into the tissue was slightly increased while the uptake into the RBCs was severely reduced, which resulted in an increased Tissue/RBC ratio compared with those in healthy subjects. The mean whole lung ratio values for ILD subjects were summarized in Table 4 and were all statistically significant ($p < 0.05$ for all ratio values). Moreover, there was a statistical difference ($p < 0.05$) in the mean slice Tissue/RBC ratio for all acquired MRI slices (Figure 17). These results were similar to those reported in a similar study of IPF reported by Kaushik et al. [54].

ILD subjects had a significantly smaller FVC predicted ($p < 0.05$) (Figure 18A). Nevertheless, the Tissue/RBC appeared to be a more sensitive parameter to some

pathological changes than the FVC predicted. Six of the ILD subjects had a FVC predicted within the range of 74-80%, while their Tissue/RBC had a larger dynamic range from 2.8-6.0. The ILD population also have a larger distribution of whole lung mean Tissue/RBC values compared to the healthy population (Figure 18B). The large variation in the mean Tissue/RBC values was possibly due to ILD subjects having different levels of disease severity. Hematocrits for six of the ILD subjects were acquired and were within the normal range of 40-50% (Figure 18C) [55]. However, the RBC/Gas ratio was reduced compared to healthy subjects except for one outlier, I8. This supported the hypothesis that the reduced gas transfer into the RBCs was due to gas transfer impairment and not due to loss of RBCs. The T2* and chemical shift for the tissue and RBC components were not statistically significant between healthy and ILD subjects. The calculated values were similar to those reported in literature.

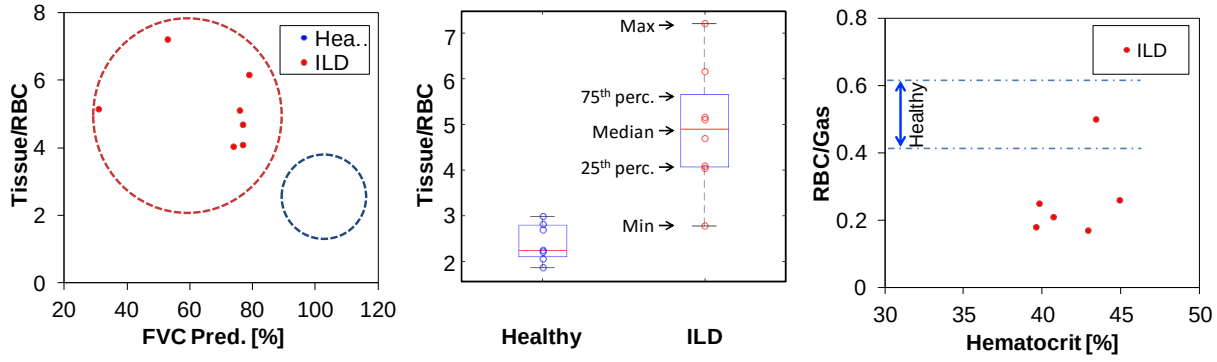

Figure 18: (A) Whole Lung Mean Tissue/RBC vs. FEV_1 predicted. (B) Box and whisker plots for the Whole Lung Mean Tissue/RBC. (C) Whole Lung Mean RBC/Gas vs. Hematocrit for 6 ILD subjects.

3.B.3 Discussion

From this preliminary study, we found that ILD subjects had a significantly higher Tissue/RBC ratio compared to that of healthy subjects. This was due to ILD subjects having an increased Tissue/Gas ratio and decreased RBC/tissue ratio by a factor of 2 compared to that of healthy subjects. Having a measured parameter with a large dynamic range was desirable because it allowed for the detection of small pathological

changes within the lungs [56]. However, it was important to recognize other potential factors that could cause variations in the measured parameter.

More specifically, Qing et al. found that the inflation level of the lungs had a strong impact on the measured ratios [56]. From maximum deflation at the lung residual volume (RV) to maximum lung inflation at the total lung capacity (TLC), the RBC/Gas ratio decreased by as much as 250% while the Tissue/Gas ratio decreased by 120%. While the total mass of lung tissue did not change during the respiratory cycle, the tissue was stretched as the lungs were inflated, which resulted in a decreased tissue density and lower measured Tissue/Gas ratio. On the other hand, the decrease in the RBC/Gas ratio could be due to a stretch-induced increase in capillary flow resistance. To minimize inflation level dependent variations, all subjects were administered a volume of gas equal to 1/3 of their measured FVC by spirometry and were asked to hold their breath for the entire duration of the scan. However, this solution was not ideal since it was highly dependent on subject cooperation and effort. A potential alternative method was to retrospectively determine the lung inflation level by comparing the matching proton images acquired during the same breath hold as the 3D-SBCSI acquisition to proton images of the lungs at RV and TLC. A correction in the post processing could be applied to remove inflation level dependent variations.

One limitation of this preliminary study was that the healthy subjects (average age: 29 ± 12 years old) imaged were not age-matched with the ILD subjects (average age: 66 ± 22 years old). While the exact effect of age on the measured ratio values was not known, it was expected that younger individuals would have better ventilation and gas uptake and exchange throughout the lungs compared to elderly individuals. For healthy subjects (age: 20-26 years old, N = 7) the average Tissue/RBC ratio was 2.3 ± 0.36. The oldest healthy subject, H4, (age: 52 years old, N = 1) had a Tissue/RBC ratio of 2.9, which was 29% greater than the mean Tissue/RBC ratio of the younger healthy population. Nevertheless, even after increasing each young healthy Tissue/RBC ratio by 29%, there was a statistical significance in the Tissue/RBC ratio between the adjusted healthy and ILD subjects, $p < 0.05$.

3.C. New Peak Identified in Lung Cancer Subject

The multi-peak detection algorithm did not detect any new peaks in addition to the known gas, tissue, and RBC peaks, in the healthy and ILD subjects. However, in a small pilot study of 3 different lung cancer (LC) subjects, the algorithm detected one new peak in subject LC1.

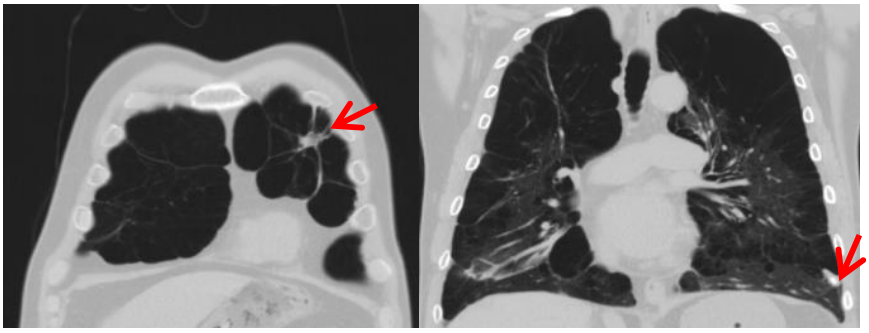

Figure 19: HRCT images for subject LC1 to illustrate the location of the two tumors as denoted by the red arrow. The tumors are located at the top anterior position of the lungs and the other one is more posterior at the bottom of the lungs.

This subject had two prominent tumors that were identified using clinical HRCT images. One of the tumors was located at the upper lobe anterior position of the lungs and the other one was more posterior at the lower lobe of the lungs (Figure 19). Of those two tumors, the new peak was found in voxels at the location of the more posterior tumor in the lower lobe of the lungs and was not found anywhere else in the lungs (Figure 20). In the tumor spectrum, the new peak was located at 97 ppm in the second and third slices of the 3D-SBCSI data.

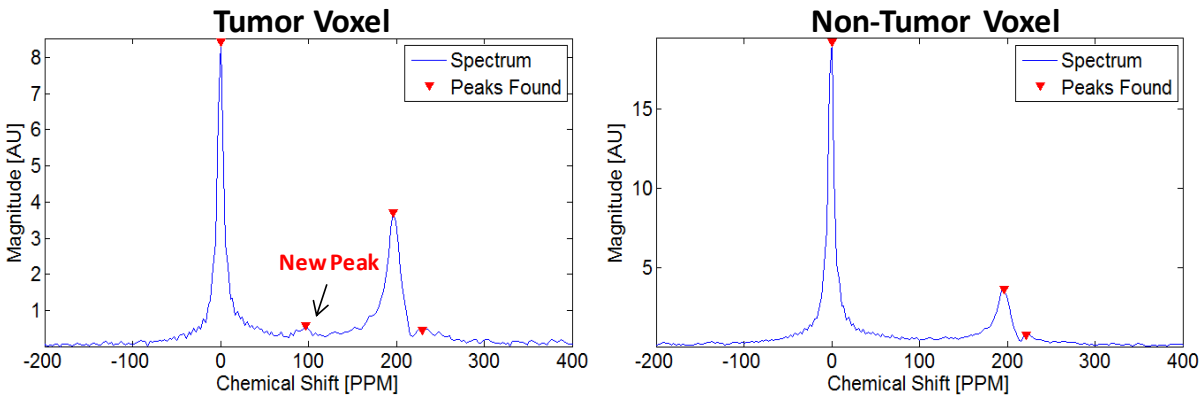

Figure 20: Representative spectra of a voxel from the posterior tumor location and another voxel from a non-tumor location in subject LC1.Both spectra had peaks corresponding to the gas, tissue and RBCs. However, a new peak at 97 ppm could only be seen in the tumor spectrum.

Similar to the other peaks, the new peak was also quantified on a per voxel basis to generate a 3D-SBCSI map. Different levels of thresholding was applied to the map as described by equation (3). With a low threshold, several regions of voxels were identified to contain the new peak (Figure 21C) in both slices. An increased threshold resulted in a decreased number of these regions (Figure 21D). A threshold of five resulted only in one region and higher thresholds resulted in an empty map (Figure 20E). The 3D-SBCSI maps of the new peak were fused with proton images that were acquired within the same breath hold as the 3D SB-CSI acquisition (Figure 21A). The location of the tumor in the proton images appeared to be well localized with the "hot spot" in the CSI map of the new peak for the two contiguous slices (Figure 21B).

Differences in the location of the tumor between the proton images and CSI map was possibly due to variations in the lung inflation level and error in registering the images. While the 3D-SBCSI and protons were acquired in the same breath hold, it was difficult for a diseased subject to hold his breath completely still for the entire duration of the acquisition.

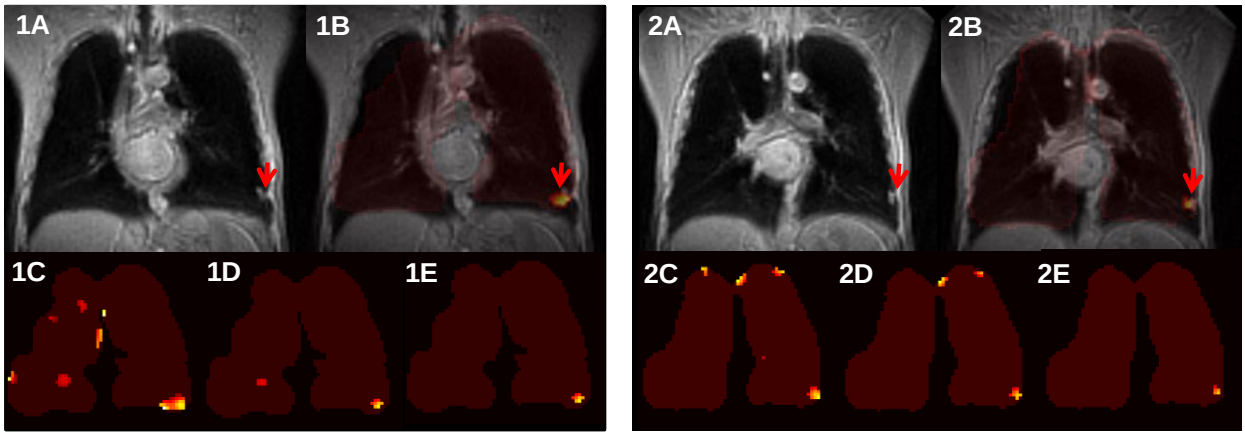

Figure 21: Contiguous slices showing the posterior lung tumor from subject LC1. 3D-SBCSI maps of the new peak at different levels of thresholding. (1A-1E) Second slice and (2A-2E) Third slice of the 3D-SBCSI maps. (A) Proton image acquired during the same breath hold as the 3D-SBCSI acquisition from subject LC1. The red arrow denotes the location of the posterior tumor. (B) 3D-SBCSI "New Peak" map fused with the same proton image as in "A" with the red arrow denoting the location of the tumor. (C) Threshold of one. (D) Threshold of three. (E) Threshold of 5.

The new peak was not detected in voxels of the upper lobe anterior tumor possibly due to the poor SNR of spectra located in the most anterior slice of the lungs. Another plausible explanation was that the peak appeared only in the presence of specific tumor types. Given that the new peak was found in voxels only near or on the tumor, it was likely that the new peak is associated with the presence of a tumor. However, the underlying factors that caused a peak to at this frequency was not known. Nevertheless, this new peak was only detected in one subject. The new peak had the highest SNR at the 6 months post radiation time point, but peaks in the range of 97±17 ppm were observed at 3 and 12 months post radiation as well. Additional studies are required to confirm the repeatability and origins of the new peak.

In summary, a total of 17 subjects (6 healthy, 8 ILD, and 3 LC) underwent 3D-SBCSI in this study. ILD subjects had a higher whole lung mean Tissue/RBC and Tissue/Gas and a lower whole lung mean RBC/Gas than that of healthy subjects (Figure 16). There was a statistically significant difference in the three different whole lung mean ratios between ILD and healthy subjects ($p < 0.05$) (Table 4). Moreover, ILD subjects also had a statistically significant higher mean Tissue/RBC for all acquired MR

slices ($p < 0.05$ for all slices) (Figure 17). In comparison to the FVC predicted from spirometery, the Tissue/RBC appeared to be a more sensitive parameter in detecting pathophysiological changes (Figure 18A). The ILD population had a larger distribution of whole lung mean Tissue/RBC values, while the healthy population had a tighter distribution with less variation (Figure 18B). This was possibly due to the varying level of disease severity in the ILD subjects imaged. Hematocrits were acquired for 6 of the ILD subjects, and were all within a healthy range. However, all but one of the ILD subjects presented a lower than normal mean RBC/Gas (Figure 18C). This indicated that the reduction in the mean RBC/Gas was not due to a loss of RBC, but was likely due to impaired gas exchange from the tissue into the RBC compartment.

Two potential factors unaccounted for in this study were the effects of age and variations in lung inflation level. Future studies with age matched healthy subjects and a post-processing correction for lung inflation level is needed to account for these factors.

Among the three LC subjects imaged, a new peak at 97 ppm was identified in subject LC1 (Figure 20). This particular subject was imaged at 4 different time points at 1, 3, 6, and 12 months after receiving radiation treatment. The new peak had the highest SNR and could be easily seen at the 6 months post radiation time point. However, peaks within the range of 97±17 ppm were observed at the 3, 6, and 12 months post radiation. Although, subject LC1 had two tumors, only the posterior one was detected using 3D-SBCSI. Nevertheless, the new peak only appeared in spectrums of voxels either near or on the posterior tumor. After quantifying this new peak and fusing the resulting CSI map with matching proton images, the tumor in the CSI map appeared to localize well with the tumor in the proton images in two contiguous slices (Figure 21). Additional studies with LC subjects are required to demonstrate the repeatability of this new peak and better understand its origins.

Chapter 4: Conclusion

Hyperpolarized Xe-129 imaging has enabled many unique approaches for evaluating lung structure and function. This preliminary work focused on the application of 3D-SBCSI, a technique pioneered by the HP Gas research group at the Department of Radiology and Medical Imaging at the University of Virginia. 3D-SBCSI used a combination of MR spectroscopy imaging and hyperpolarized Xe-129 to exploit xenon's high solubility in biological tissues and ability to produce MR spectral peaks with distinct resonant frequencies.

In this work, we presented a robust post processing software package termed "Tools for Automated Spectral Processing" (TASP) for automated processing and quantification of MR spectroscopy data. TASP used a Lorentzian line fitting method to quantify the different peaks detected within the spectrum (Figure 8 and 9). This approach was shown, through simulations, to be a superior technique compared to the area integration method. Three different simulations were performed including: shifting the RBC peak, varying the simulated Tissue/RBC ratio, and varying the SNR of the spectrum, to compare the accuracy and robustness of the fitting and area integration methods (Figurs 12-13). We demonstrated that the area integration method was less accurate in differentiating and quantifying the tissue and RBC compartments. On average, the area integration method had an error of 27% in quantifying the Tissue/RBC ratio. On the other hand, the line fitting method had an error of ~3% for a physiologically relevant range of RBC peak shifts and typical SNR levels of a real spectrum from healthy or diseased subjects.

From this preliminary work, we demonstrated the feasibility of 3D-SBCSI for assessing regional lung ventilation and gas uptake and exchange in 3D within a single breath hold (less than 10 seconds). Healthy subjects typically showed a uniform distribution of gas signal intensities and Tissue/RBC ratios throughout the lungs. Whereas, ILD subjects showed a heterogeneous distribution (Figure 16). The Tissue/RBC ratio maps of ILD subjects had several regions of elevated ratio values, which indicated regions of impaired gas transfer between the tissue and RBC

compartments. Impairment of gas exchange was likely due to the presence of honeycombing and fibrosis in ILD subjects. Overall, ILD subjects typically had a statistically significant higher Tissue/RBC ratio ($p < 0.05$) due to a higher Tissue/gas and lower RBC/Gas ratio compared to those of healthy subjects, Table 2. Moreover, a clear statistically significant difference in the mean Tissue/RBC ratio was seen for each acquired MRI slices ($p < 0.05$) (Figure 17). However, more studies with age matched healthy subjects are required to fully validate the findings from this preliminary study. Nevertheless, having this unique regional structural and functional information may allow for improved detection, monitoring, and understanding of pulmonary diseases.

Unlike other dissolved phase imaging techniques, 3D-SBCSI acquired the full spectrum for each voxel, which allowed for the detection of potentially new peaks in diseased subjects. In a preliminary study of 3 LC subjects, a new peak located at 97 ppm corresponding to the presence of a tumor was found in one subject (Figure 20). This new peak was only seen in spectra of voxels located on or near the tumor. After quantifying and mapping the new peak, the "hot spot" located in the 3D-SBCSI maps of the new peak was well co-localized with the tumor of the proton images in two contiguous slices (Figure 21). However, the same subject also had a second tumor in the anterior upper lobe of the lungs that could not be detected, possibly due to the poor SNR of spectra located in the most anterior slice of the lungs. On the other hand, it was possible that this peak was associated with a specific type of lung tumors, which could help explain why the same peak was not detected in the other LC subjects. Additional studies are required to confirm the repeatability and origins of the new peak.

Although, quantification of the spectra was improved, quantitative interpretations of the results were largely limited to comparing whole lung and slice mean values between subjects. Comparing means was a straightforward approach, but it ignored the spatial information and emergent patterns within an image. This information could be used to improve the sensitivity of the technique to identify subtle regional differences that may be useful in understanding disease progression. Machine learning and image texture analysis techniques applied in analyzing CT images should be explored in the future for analyzing 3D-SBCSI images [57-59].

References

[1] Hornak J. *The Basics of MRI*. 2011. Web. 27 Oct 2015.

[2] Fain, S.B., et al., *Functional lung imaging using hyperpolarized gas MRI*. JMRI, 2007. 25(5):910-23.

[3] Theilmann RJ, Arai TJ, Samiee A, Dubowitz DJ, Hopkins SR, BuxtonRB, Prisk GK. *Quantitative MRI measurement of lung density must account for the change in T2* with lung inflation*. J. Magn. Reson.Imaging, 2009. 30: 527–534.

[4] Miller GW, Mugler JP 3rd, Sa RC, Altes TA, eat tal. *Advances in functional and structural imaging of the human lung using proton MRI*. NMR Biomed, 2014. 27(12):1542-56.

[5] Mugler JP 3rd, Altes TA. *Hyperpolarized Xe129 MRI of the Human Lung.* J Magn Reson Imaging, 2013. 37(2):313-331.

[6] Salerno M, Altes TA, Mugler JP III, Nakatsu M, Hatabu H, de Lange EE. *Hyperpolarized noble gas MR imaging of the lung: potential clinical applications*. Eur J Radiol, 2001. 40:33–44.

[7] Matsuoka S, Patz S, Albert MS, et al. *Hyperpolarized gas MR imaging of the lung: current status as a research tool*. J Thorac Imaging, 2009. 24:181–188.

[8] Fain S, Schiebler ML, McCormack DG, Parraga G. *Imaging of lung function using hyperpolarized helium-3 magnetic resonance imaging: review of current and emerging translational methods and applications*. J Magn Reson Imaging, 2010. 32:1398–1408.

[9] Sun, Y., et al., *Using hyperpolarized 3He MRI to evaluate treatment efficacy in cystic fibrosis patients*. Journal of Magnetic Resonance Imaging, 2011. 34(5):1206-11.

[10] Fain, S.B., et al., *Functional lung imaging using hyperpolarized gas MRI*. Journal of Magnetic Resonance Imaging, 2007. 25(5):910-23.

[11] Ruset, I.C., S. Ketel, and F.W. Hersman, *Optical pumping system design for large production of hyperpolarized Xe-129*. Phys Rev Lett, 2006. 96(5).

[12] Hersman, F.W., et al., *Large production system for hyperpolarized 129Xe for human lung imaging studies*. Acad Radiol, 2008. 15(6):683-92.

[13] Miller KW, Reo NV, Schoot Uiterkamp AJ, Stengle DP, Stengle TR, Williamson KL. *Xenon NMR: chemical shifts of a general anesthetic in common solvents, proteins, and membranes*. Proc Natl Acad Sci USA, 1981. 78:4946–4949.

[14] Sakai K, Bilek AM, Oteiza E, et al. *Temporal dynamics of hyperpolarized 129Xe resonances in living rats*. J Magn Reson, 1996. 111:300–304.

[15] Ruppert K, Brookeman JR, Hagspiel KD, Mugler JP III. *Probing lung physiology with xenon polarization transfer contrast (XTC)*. Magn Reson Med, 2000. 44:349–357.

[16] Wagshul ME, Button TM, Li HF, et al. *In vivo MR imaging and spectroscopy using hyperpolarized 129Xe*. Magn Reson Med, 1996. 36:183–191.

[17] Mugler JP III, Driehuys B, Brookeman JR, et al. *MR imaging and spectroscopy using hyperpolarized 129Xe gas: preliminary human results*. Magn Reson Med, 1997. 37:809–815.

[18] Ruppert K, Brookeman JR, Hagspiel KD, Driehuys B, Mugler JP III. *NMR of hyperpolarized 129Xe in the canine chest:spectral dynamics during a breath-hold*. NMR Biomed, 2000. 13:220–228.

[19] Swanson, S.D., et al., *Distribution and dynamics of laser-polarized (129)Xe magnetization in vivo*. Magnetic Resonance in Medicine, 1999. 42(6):1137-45.

[20] Cleveland ZI, Cofer GP, Metz G, et al. *Hyperpolarized 129Xe MR imaging of alveolar gas uptake in humans*. PLoS ONE, 2010. 5:12192.

[21] Mugler JP III, Altes TA, Ruset IC, et al. *Simultaneous magnetic resonance imaging of ventilation distribution and gas uptake in the human lung using hyperpolarized xenon-129*. Proc Natl Acad Sci USA, 2010. 107:21707–21712.

[22] Driehuys, B., et al., *Imaging alveolar-capillary gas transfer using hyperpolarized Xe-129 MRI*. Proceedings of the National Academy of Sciences of the United States of America, 2006. 103(48):18278-18283.

[23] Qing K, Ruppert K, Jiang Y, Mata JF, Miller GW, Shim YM, et al. *Regional mapping of gas uptake by blood and tissue in the human lung using hyperpolarized xenon-129 MRI*. J Magn Reson Imaging, 2014. 39(2):346–59.

[24] Mata, J., et al., *High-Resolution Chemical Shift Imaging of the Lungs with Xe-129 During a Single 6 Second Breath-Hold: Results from a Rabbit Model of Pulmonary Embolism.* Proceedings of the International Society of Magnetic Resonance in Medicine, 2008. 16:2679.

[25] Mata, J., et al., *Chemical Shift Imaging of the lungs with hyperpolarized Xe-129: Results from a rabbit model of stereotactic lung radiosurgery with and without a radioprotector.* Proceedings of the International Society of Magnetic Resonance in Medicine, 2009. 17:2211.

[26]Mata, J., et al., *Quantification and temporal study of physiologic lung changes in animal models of lung disease using 2D and 3D-CSI with Xe-129.* Proceedings of the International Society of Magnetic Resonance in Medicine, 2010. 18:989.

[27] Mata, J., et al., *Improved Separation and Quantification of Xe-129 Dissolved-Phase Resonances in the Lung.* Proceedings of the International Society of Magnetic Resonance in Medicine, 2011. 19:884.

[28] Guan S., Qing K., Altes T., et al. *Regional Quantification of Lung Function in Cystic Fibrosis using 3D Single-Breath Chemical Shift Imaging*. Abstract# 4400. Presented at the 22nd Annual Meeting ISMRM, 2014. Milan.

[29] Nagashima, K., *Optimum pulse flip angles for multi-scan acquisition of hyperpolarized NMR and MRI.* J Magn Reson, 2008. 190(2):183-8.

[30] Cleveland, Z.I., et al., *Hyperpolarized (129)Xe MR Imaging of Alveolar Gas Uptake in Humans.* Plos One, 2010. 5(8).

[31] Chang, Y., Quirk, J., Ruset, I., et al., *Quantification of Human Lung Structure and Physiology using Hyperpolarized 129Xe*. Magn Reson Med, 2014. 71(1):399-44.

[32] . Verma S, Rajesh A, Futterer JJ, et al. Prostate MRI and 3D MR spectroscopy: how we do it. AJR Am J Roentgenol, 2010. 194: 1414–1426.

[33] Posse, S., Otazo, R., Dager S., Alger, J., *MR Spectroscopic Imaging: Principles and Recent Advances*. J Magn Reson Imaging, 2013. 37(6):1301-25.

[34] Jean-Baptiste Poullet, Diana M. Sima, Sabine Van Huffel. *MRS signal quantitation: A review of time- and frequency-domain methods*. JMR, 2008. 195: 134-144.

[35] Keeler, J., *Understanding NMR Spectroscopy,* 2005. John Wiley & Sons Ltd.

[36] Hornak, J. *The Basics of NMR*, 1999. https://www.cis.rit.edu/htbooks/nmr/inside.htm. Web. 01 Sept. 2015.

[37] Mierisová, Š. and Ala-Korpela, M., MR spectroscopy quantitation: a review of frequency domain methods. NMR Biomed, 2001. 14: 247–259.

[38] Bernstein, M., Fain B., Reiderer, S., *Effect of windowing and zero-filled reconstruction of MRI data on spatial resolution and acquisition strategy*. J. Magn Reson Imaging, 2001. 14:270-280.

[39] McRobbie DW. *MRI from Picture to Proton*. 2003.

[40] Fay M., Proschan M. *Wilcoxon-Mann-Whitney or t-test? On assumptions for hypothesis tests and multiple interpretations of decision rules.* 2010. Stat Surv. 4:1-39.

[41] Wilcoxon F. *Individual comparisons by Ranking Methods.* Biometrics Bulletin, 1945. 1:80-3.

[42] Wallis A, Spinks K. *The diagnosis and management of interstitial lung diseases*. BMJ, 2015. 350.

[43] Ley B, Collard H, King T, et al. *Clinical course and prediction of survival in idiopathic pulmonary fibrosis*. *Am J Respir Crit Care Med,* 2011. 183:431-40.

[44] Lamas DJ, Kawut SM, Bagiella E, et al. *Delayed access and survival in idiopathic pulmonary fibrosis: a cohort study*. *Am J Respir Crit Care Med,* 2011. 184:842-7.

[45] The Idiopathic Pulmonary Fibrosis Clinical Research Network. *Randomized trial of acetylcysteine in idiopathic pulmonary fibrosis*. *N Engl J Med,* 2014. 370:2093-101.

[46] National Institute for Health and Care Excellence. *Pirfenidone for treatment idiopathic pulmonary fibrosis*. (Technology appraisal guidance 282.) 2013.

[47] Mcleod T, Carrington C, Gaensler E. *Diffuse interstitial lung disease: a new scheme for description*. *Radiology,* 1983. 149:353-63.

[48] Raghu G, Collard H, Egan J, et al. *An Official ATS/ERS/JRS/ALAT statement: idiopathic pulmonary fibrosis: evidence-based guidelines for diagnosis and management*. *Am J Respir Crit Care Med,* 2011. 183:788-824.

[49] de Jong PA, Long FR, Nakano Y. *Computed tomography dose and variability of airway dimension measurements: how low can we go?* Pediat Radiol, 2006. 36:1043–7.

[50] Brenner D, Elliston C, Hall E, et al. *Estimated risks of radiation-induced fatal cancer from pediatric CT*. AJR, 2001. 176:289–96.

[51] Gustafsson P, de John PA, Tiddens H, et al. *Multiple-breath inert gas washout and spirometry versus structural lung disease in cystic fibrosis*. Thorax, 2008. 63:129-134.

[52] Cleveland ZI, Cofer GP, Metz G, et al. *Hyperpolarized 129Xe MR imaging of alveolar gas uptake in humans*. PLoS ONE, 2010. 5:e12192.

[53] Mugler JP III, Altes TA, Ruset IC, et al. *Simultaneous magnetic resonance imaging of ventilation distribution and gas uptake in the human lung using hyperpolarized xenon-129*. Proc Natl Acad Sci USA, 2010. 107:21707–21712

[54] Kaushik, S., Freeman, M., Yoon, Suk, et al. *Measuring Diffusion-Limitation with a Perfusion-Limited Gas-Hyperpolarized Xe129 Gas-Transfer Spectroscopy in Patients with Idiopathic Pulmonary Fibrosis.* J appl physio, 2014. 117(6):577-85.

[55] Lichtman MA, et al. *Williams Hematology*. 8th ed. New York, N.Y.: The McGraw-Hill Companies; 2010.

[56] Qinq K., Mugler JP III, Altes TA, et al. *Assessment of lung function in asthma and COPD using hyperpolarized 129Xe chemical shift saturation recovery spectroscopy and dissolved phase MRI*. NMR Biomed, 2014. 27(12):1490-501.

[57] Ganeshan B, Abaleke S, Young RCD, Chatwin CR, Miles KA. *Texture analysis of non-small cell lung cancer on unenhanced computed tomography: initial evidence for a relationship with tumour glucose metabolism and stage*. Cancer Imaging. 2010. 10(1):137-143.

[58] Alic L, Niessen WJ, Veenland JF. *Quantification of Heterogeneity as a Biomarker in Tumor Imaging: A Systematic Review*. Hatzis C, ed. *PLoS ONE*, 2014. 9(10):e110300.

[59] Hunter LA, Krafft S, Stingo F, et al. *High quality machine-robust image features: Identification in nonsmall cell lung cancer computed tomography images*. Medical Physics, 2013. 40(12):121916.